Theoretical and Applied Fracture Mechanics 134 (2024) 104730

Contents lists available at ScienceDirect

Theoretical and Applied Fracture Mechanics

journal homepage: www.elsevier.com/locate/tafmec

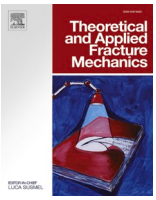

Characterisation of 18Ni 300 steel CT specimens in a fatigue test manufactured by selective laser melting at 0°, 45° and 90°

Pablo M. Cerezo [a], Alejandro S. Cruces [a], Steven Moore [b], Greg Wheatley [b], Pablo Lopez-Crespo [a,*]

[a] Department of Civil and Materials Engineering, University of Malaga, C/Dr Ortiz Ramos, s/n, 29071 Malaga, Spain
[b] College of Science and Engineering, James Cook University, Douglas, Queensland 4811, Australia

ARTICLE INFO

Keywords:
Additive Manufacturing (AM)
Fatigue crack growth
Maraging steel
Porosity
Selective Laser Melting (SLM)

ABSTRACT

Maraging steel, 18Ni300, is a high-performance material that shows promising potential for various industrial applications. Selective Laser Melting is utilized in the manufacturing of high-value components. Understanding the fatigue mechanisms of this material is imperative, as its fatigue life is influenced by both surface and internal porosity, as well as defects produced when manufacturing the objects due to the patterns used. The main objective is to analyze the characterization of these pores and clarify their relationship with the fatigue properties of the material under study. Compact tension specimens were manufactured by selective laser melting at three angles (0°, 45° and 90°) with respect to the crack growing direction and fatigue tests were performed. A study of the porosity of the sample was conducted, which established a correlation between the printing angle, growing rate (da/dN curves), and the porosity that is categorised through the aspect ratio and the circularity ratio. It is shown that all manufacturing orientations generate similar pore sizes and area, but the 45° orientation induces pore with slightly higher circularity ratio. The results indicate that the faster fatigue crack growth might be linked to the slight increase in pore area and circularity, and this was observed for 45°.

1. Introduction

Additive Manufacturing (AM) is a highly advantageous process that entails creating a three-dimensional structure by gradually constructing two-dimensional layers. This innovative approach offers significant benefits over conventional manufacturing techniques, such as material subtraction [1]. Creating complex parts quickly and efficiently while using minimal materials makes it perfect for rapid prototyping and manufacturing [2].

One promising method of AM is Selective Laser Melting (SLM). Its impressive capabilities include the production of high surface quality items, consistent repeatability, and moderate speed, all of which make it a popular choice for a wide range of applications. This technology is poised for a bright future as it continues to advance and evolve [3,4].

Several studies [5,6,7] have explored the fatigue behaviour in ductile metallic materials, with a specific emphasis on titanium and aluminium alloys produced by AM techniques. Although the fatigue behaviour of maraging steel has also been studied in the past [8,9], there is still a need to expand our knowledge in order to better understand its mechanical properties and potential applications. The increasing use of AM means that knowledge of its mechanical properties is essential both for prototypes (that are likely to be tested extensively) and for components (that will undergo less extensive testing, e.g. replacement parts).

When utilising this manufacturing methodology for creating intricate components, it is imperative to conduct a thorough examination of the fracture mechanics associated with the various materials that are being processed. Gaining a comprehensive understanding of how cracks manifest within a given material, as well as the extent to which it can withstand damage before reaching a critical failure point, is paramount to maximising the longevity of the manufactured parts [10].

Fatigue life depends on the material properties and the environment, such as temperature, humidity, oxidation, surface finish, or loading conditions [11]. differe. AM results in an anisotropic material with directional grain structures and residual stresses that affect crack growth behaviour. The angle between the part impression and the load application determines how the crack growth will behave.

Directional or columnar grain structures have different mechanical properties depending on the orientation forces applied through the

* Corresponding author.
E-mail address: plopezcrespo@uma.es (P. Lopez-Crespo).

https://doi.org/10.1016/j.tafmec.2024.104730
Received 30 November 2023; Received in revised form 19 October 2024; Accepted 20 October 2024
Available online 22 October 2024

Table 1
Chemical composition of 18Ni300 steel.

[wt/%]	Fe	C	Cu	Cr	Al	Ti	Mo	Co	Ni (%)
18Ni300	Balance	≤0.3	≤0.5	≤0.5	0.05–0.15	0.6–0.8	4.5–5.2	8.5–9.5	17–19

Table 2
Main properties of 18Ni300 steel [24].

Young's modulus (GPa)	Tensile strength (MPa)	Yield strength (MPa)	Density (kg/m^3)	Vickers hardness
168	1147	910	7420	352.7

material [12]. Because each layer is produced with a time interval, the grain structure may lack adhesion between these layers, weakening it. Some authors [13] show how martensitic grains are presented in an SLM sample and how they form the structure of the specimen [14] in different growing directions [15]. Further analysis is needed to fully understand the correlation between microstructure and fatigue stresses.

According to Wu and co-authors [16] fatigue crack growth tests on SLM manufactured samples showed a behaviour dependent on the direction of grain growth that coincides with the printing path. It was observed that grains oriented in the direction of a crack exhibit greater resistance to fatigue crack growth. However, no investigation and analysis of defects in such samples was carried out, and no additional investigation was performed with different printing directions. The effect of defect size on the fatigue life was studied recently and for a material such as AlSi10Mg, the defect size was found to be a first-order parameter that controls the fatigue limit. [17] They also observed that the direction of construction had no impact on the fatigue strength of the material, which contrasts with what other research such as ([16] or [18]) concluded. This may be due to the fact that the manufacturing method is not the same (SLM or laser power bed) or due to the lack of a parallel study besides the S-N curves. The differences between the printing directions on 18Ni300 steel were analysed based on surface data of crack initiation [18]. Unlike in the current work, the authors did not take into account the influence of the pores on the crack growth once the crack started to propagate.

The porosity of specimens built by additive manufacturing was previously investigated, though the porosity analysis was not linked to fatigue behaviour [19,20].

The current work is more comprehensive than the previous work. While some of the previous works [21,22] carry out a fatigue study in some directions but do not relate it to the porosities, other works investigate the porosity effect but do not relate them to the fatigue behaviour in the different printing directions [23]. Therefore, in this work, the study is performed in three manufacturing directions with respect the crack propagation plane. Moreover, the current study also includes a thorough analysis of porosities in the manufactured specimens and investigates their impact on the microstructure and hence on the fatigue behaviour.

2. Materials and methods

2.1. Material

An 18Ni300 steel powder is used as the base material for SLM. The powder is melted layer by layer using a high-power laser in the LPBF process to create Compact Tension Test (CT) specimens via Lasercusing®. The use of Renishaw's AM 400 equipment model in LPBF processes, combined with the optimization of process parameters, resulted in the desired outcomes. The process uses a laser power of 400 W, a scan speed of 0.85 m/s, and a laser diameter of 0.04 mm. The deposited layer is 30 μm thick, with a hatch spacing of 100 μm and a 25

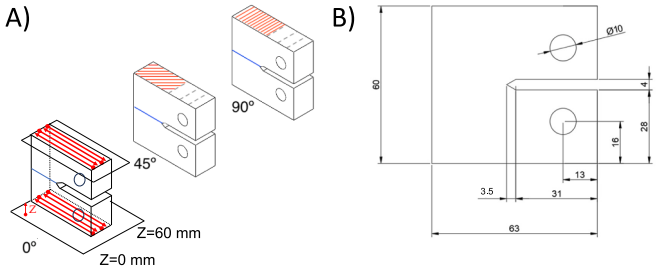

Fig. 1. A) AM Layer Orientation Angle (Red lines are layer orientation, blue lines are crack planes) and B) geometry of the CT Specimen Manufacturing.

% overlap. No post-treatment procedure is conducted. Tables 1 and 2 show the chemical composition and main properties of the powder provided by the manufacturer. CT specimens were produced using varying orientations: 0°, 45°, and 90°. These angles indicate the anticipated direction of crack propagation, as depicted in Fig. 1a. The SLM process adhered to the pattern shown in Fig. 1a from z = 0 to z = 60 mm for each orientation, and the specimens were further modified by machining notches and holes.

As indicated in Table 2, the uniaxial tensile test response of the bulk material shows a Young's modulus of 168 GPa. Notably, this figure is lower than the corresponding Young's modulus for the wrought material [25] and falls substantially below the typical benchmark of 210 GPa. Similar differences between the wrought material and the additively manufactured material were observed previously [26,27,28,29,30]). The variance is ascribed to the effect of the porosity of the samples that is determined by the printing parameters employed. Furthermore, the heat treatment procedure also appears to have a high influence on Young's modulus [31].

2.2. Fatigue experiment methods

The samples under examination were produced through AM in three different directions: 0°, 45°, and 90°, with respect to the axis of the plane that is orthogonal to the fracture plane, as shown in Fig. 1a. The selection of these angles was based on the observation that crack growth behavior varies significantly depending on the orientation of the printed layers. Initially, it was found that varying the printing angle of the layer combination enhances material properties. However, this is not always feasible due to the geometry of some parts, which require consistent layer orientation. Therefore, three main directions were chosen for study.

Before performing either type of test, the CT specimens were precracked to allow for a more natural crack pattern to occur during the test. Additionally, the surface was polished to enhance the precision of crack position determination. The surface roughness measurements showed an Ra range of 1.05 to 1.72 μm and an Rq range of 1.35 to 1.72 μm.

The experiments followed ASTM the E399 standard test method for linear-elastic plane-strain fracture toughness of metallic materials as a benchmark testing reference [32]. Fig. 1b illustrates the dimensions of the CT samples, with a thickness of 12 mm.

Prior to the fatigue test, a static test was conducted using the Shimadzu AGS-X 50 kN testing machine and an additional CT specimen to the ones used in the fatigue test. The test entailed applying force at a rate of 10 N/s until failure occurred. The force inducing fatigue cracking was

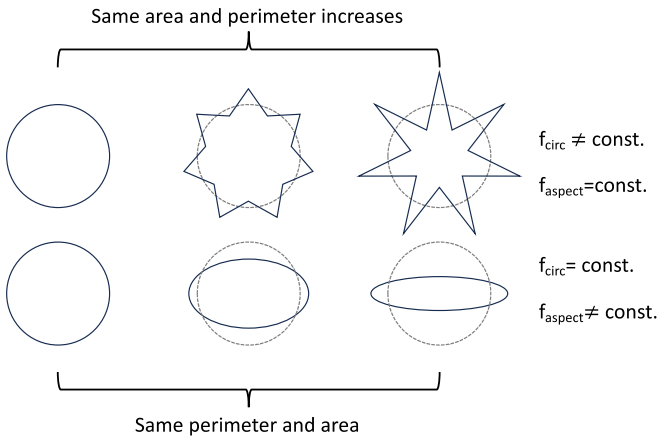

Fig. 2. Example of how circularity and aspect ratio values are affected by different geometries and irregularities.

ascertained based on the maximum load reached during the test.

The fatigue crack initiation and propagation tests were carried out using the same in-situ fatigue test machine Shimadzu AGS-X 50 kN. A camera was also installed to monitor the crack as it propagates and to allow digital measurement of the crack length as an additional data carrier.

The fatigue test was done with a cyclic load ranging from 7 to 0.7 kN. Each printed angle was subjected to a fatigue stress rate of R = 0.1. In each test, load and displacement were collected automatically every 0.01 s. MATLAB Image Viewer was then used to find the pixel length of the distance between the crack tip and the back of the CT specimen and hence the crack length. Afterwards, the Paris model is modified to fit the fatigue crack growth curves described by equation (1).

$$\frac{da}{dN} = C \cdot \Delta K^n \tag{1}$$

where da/dN is the crack growth rate, ΔK is the stress intensity factor range, and C and n are material constants determined through regression analysis. The fitting process involved applying the Paris Model to our experimental data to derive the constants C and m.

2.3. Characterisation methods

The cross-section of the three samples is examined by a high-quality microscope, obtaining an accurate assessment of microstructure and porosity. The standard metallographic practice outlined in ASTM E407-99 [33] was followed to prepare the samples, which involved a precise chemical attack utilising Nital, a nitric acid solution with a 4 % ethyl alcohol content. Following preparation, a Leica DM6 M optical microscope was used to view and analyse the samples carefully.

The images are post-processed in order to obtain a clearer view of the surface and the porosity that is studied for each printing orientation by a 2D microscopic study. The pore areas were obtained by a pixel counting method by commercial software, ImageJ. Each pore was characterised by two shape descriptors, namely circularity ratio ($f_{circ.}$) and aspect ratio (f_{aspect}). The shape descriptors are defined as follow:

$$f_{circ.} = \frac{4\pi A}{p^2} \tag{2}$$

where A and p are the cross-sectional area and perimeter of the pore, respectively. $f_{circ.}$ can take values $0 < f_{circ.} \leq 1$, where 1 represents a perfectly circular cross-section, Fig. 2.

The second descriptor is given by:

$$f_{aspect} = \frac{d_{min}}{d_{max}} \tag{3}$$

where d_{min} and d_{max} are the minimum and maximum orthogonal diagonal of the pore. f_{aspect} can take values $0 < f_{aspect} \leq 1$, Fig. 2.

3. Results and discussion

3.1. Metallography

The metallographic examination of the studied material is shown in Fig. 3a, 3b, and 3c through an optical micrograph of polished/etched as built specimens. The width of the welding beads is approximately 179 μm, noticeably elongated and well above the 125 % of the hatch spacing. Fig. 3a shows a specific directional deposition technique, apparent in the 0° and 90° samples, where the beads are deposited in a continuous straight line. On the other hand, Fig. 3b shows a deposition technique for a sample tilted at a 45° angle, utilising a combination of 0° and 90° beads that results in a higher melted pool boundary (MPB). Furthermore, a closer inspection of Fig. 3b reveals inconsistencies in the MPB. In Fig. 3a, 3b and 3c the discontinuous nature of the melting process is clearly observed. Such discontinuity is induced by the pulsating laser beam. A semi-elliptical shape through the axis parallel to the printing direction and the overlapping of different scan tracks (due to the inaccuracy of cutting machines) is observed in all the samples, in agreement with previous studies [14]. This semi-elliptical shape is a result of the thermal gradient that has its highest point on the front edge of the laser beam. As a result, the growth of the scan track is directly tied to the thermal gradient. This causes the scan tracks to cool more quickly on the front edge of the laser beam, which leads to their semi-elliptical shape.

The areas between the scan tracks that appear dark (Fig. 3) show the uneven distribution of alloy elements in the specimens once they are built. Additionally, the laser beam sometimes overlaps with the previous welding bead, which can result in high energy at the intersection points.

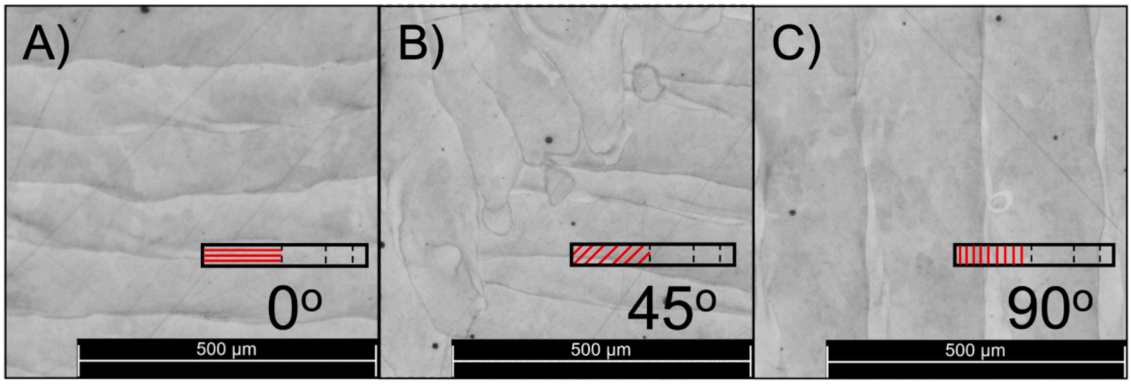

Fig. 3. Optical micrograph of maraging steel etched with Nital A) 0°, B) 45° and C) 90°.

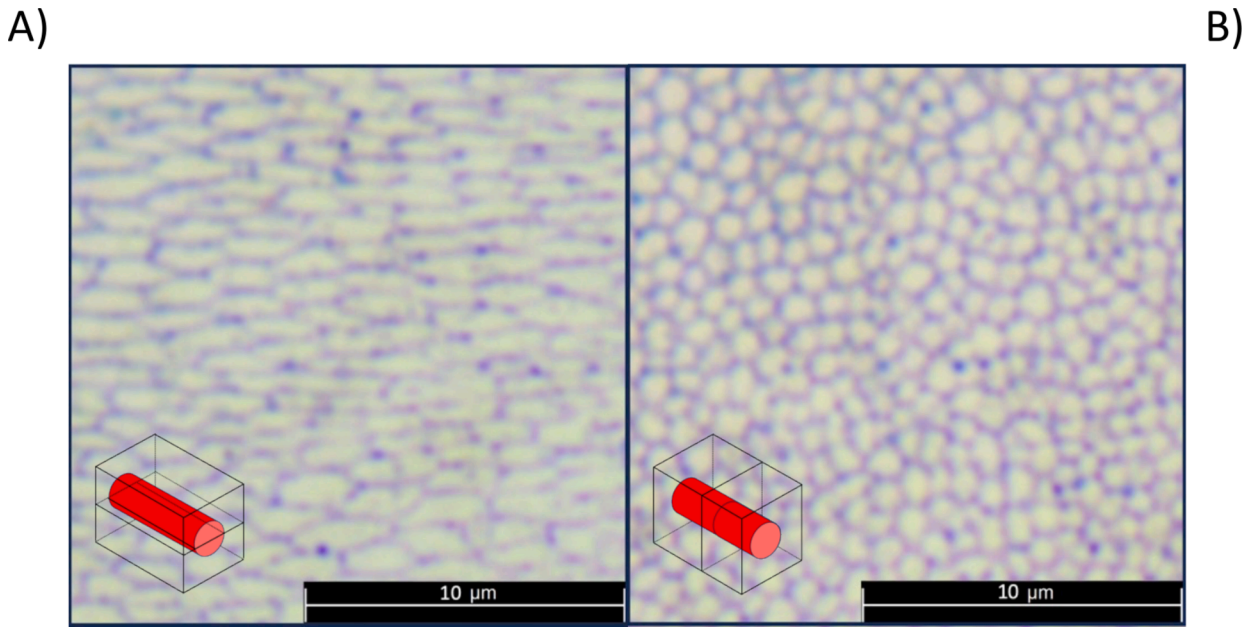

Fig. 4. A) columnar and B) dendritic structures inside maraging steel grains observed by an optical microscope.

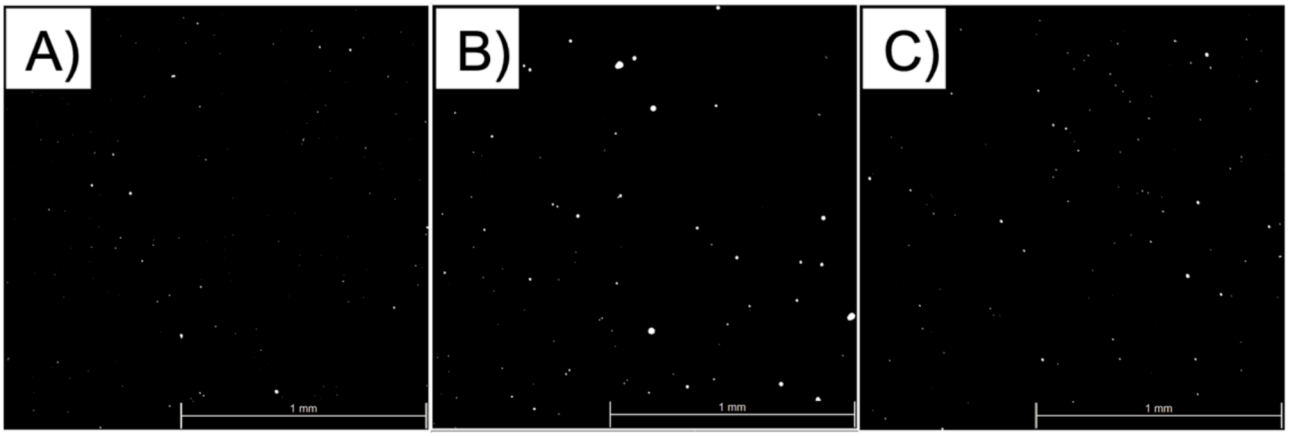

Fig. 5. Porosity area in A) 0°, B) 45° and C) 90° obtained by Leica DM6 M and post processed by ImageJ.

A cellular solidification structure is created through the complex thermal processes during SLM, and epitaxial growth also occurs across different track boundaries.

Founding grains in Fig. 3 can be challenging because cross-welding beads can cause grains to appear due to remelting when printing the next layers. Within these grains, two different structures may emerge due to differences in the growth of each bead: cellular and columnar, Fig. 4 illustrates both substructures. Fig. 4a shows an elongated cellular cells, product of cutting a dendritic cell through an angle between 0° and 90°. The vertical cross-section of the as-built specimen can be seen in 4b. Fig. 4b shows a cellular microstructure that is submicron in size and has an intercellular spacing of 1–1.5 μm. This characteristic is responsible for the remarkable strength and hardness of SLM maraging steel material.

Upon conducting an examination of the as-built specimen, it was observed that the microstructure displayed small columnar and/or dendritic grains resulting from the rapid solidification of the melt pool, as depicted in Fig. 4a. Due to the higher thermal gradients at the grain boundaries, these grains tend to extend away from them. When solidification occurred at high cooling rates, it caused the formation of α' phase and prevented the intermetallic compounds from precipitating. As a result, certain components including Ni, Co, Mo, among others, remained in a state of supersaturated solid solution [34].

3.2. Porosity

Displayed in Fig. 5a, 5b, and 5c are the percentage of porosity of the 0°, 45°, and 90° samples, respectively. These images were obtained through image treatment utilizing ImageJ software. Based on the figures, it was determined that the porosity percentages for the 0°, 45°, and 90° samples were 0.159 %, 0.193 %, and 0.150 %, respectively. As was expected, the 0° orientation and the 90° orientation have a similar percentage of porosity as the printing strategy is the same, Fig. 5a and Fig. 5c. However, when a 45° distribution is analysed, the porosity increases due to a bigger amount of grain boundaries, MPB, that promote the appearance of pores.

In Fig. 6a and 6b, two histograms represent the pore areas and the pore diameters in the sampled section for each orientation. For the purpose of measuring, a diameter equivalent to that of a circle was utilized. It is important to mention that when analyzing images, a minimum threshold can be set for the size of features, below which the pores will not be included in the count. The aim of this is to eliminate the

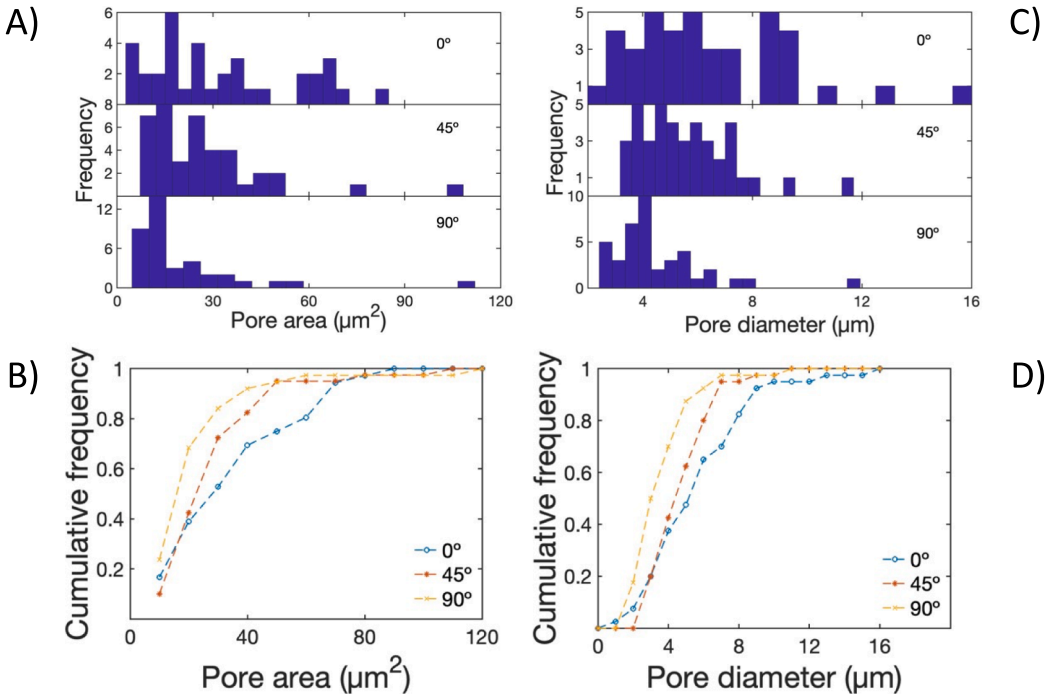

Fig. 6. Histograms representing A) pore areas and C) diameters for the 0°, 45° and 90° specimens in the as-built condition. And the cumulative frequency, normalised to the unity, of the B) pore area and D) diameters in the samples.

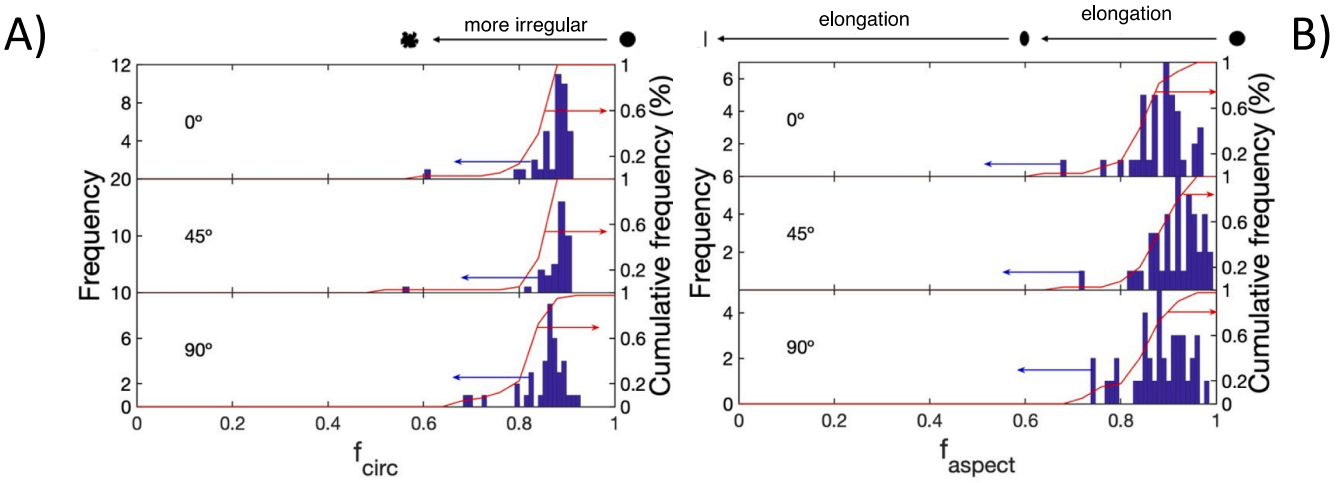

Fig. 7. Histograms and cumulative frequencies of circularity A) and aspect ratio B) of the pores in the 0°, 45° and 90° samples. These shape descriptors are defined in equations (2) and 3), respectively.

impact of experimental noise at the lower levels, which cannot be avoided even with microscopic images. The tiniest pore that could result from a disturbance is one pixel in size or 0.04 μm^2. Also, it must be outstanding that the low end, below ~ 5 μm in diameter and ~ 15 μm^2 in area dips are observed by [19] and [35] in sintered iron and steel. This is also found in these samples.

The distribution of pores in the 0° sample, Fig. 6a, shows that there is a greater number of pores with a larger area than in the 45° and 90° samples, where there are pores with a smaller area, especially in the 90° sample, where 90 % of them are less than 40 μm^2, Fig. 6b. The pore diameter distribution also shows that the 45° sample has a greater variety of diameters than the 0° sample, where there is a greater variety of diameters, Fig. 6c.

In Fig. 7 the histograms and cumulative frequencies of pore shape descriptors, f_{circ} and f_{aspect}, are provided. Circularity and aspect ratio are parameters obtained through the appliance of equations (2) and (3) for each pore. The histogram of f_{circ}, Fig. 7a, shows a narrow distribution of the circularity for 0° and 45°, but the 90° has a wider distribution showing that there is not a high smoothness of the perimeter of each pore, a circularity value close to the unity represent a perfectly circular cross-section, $f_{circ.} = \frac{4\pi A}{p^2}$. Circularity is a parameter that influences the stress concentration increasing it, the further away it is from the unit. Meanwhile, for the aspect ratio, Fig. 7b, a wider distribution is observed for all the orientations, meaning that although pores have a regular shape, their diagonals are not close to each other, $f_{aspect} = \frac{d_{min}}{d_{max}}$. The aspect ratio distribution of the 45° sample is closer to the unity than the others, thus increasing the stress concentration as it is observed in [36] and explained previously.

Fig. 8 shows the pore aspect ratio as a function of the pore area. With

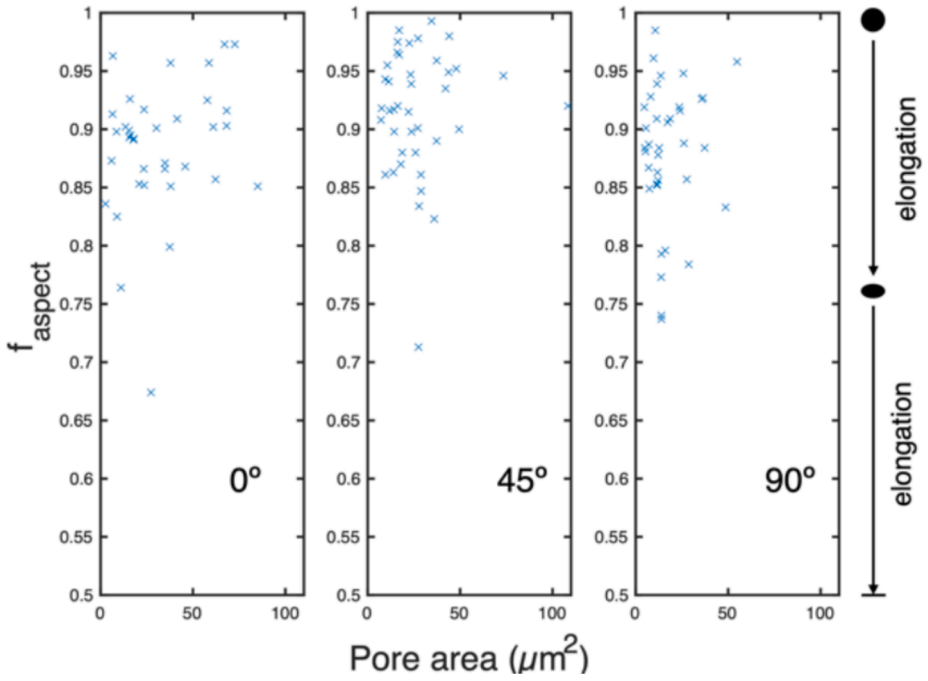

Fig. 8. Pore aspect ratios as a function of pore area in the 0°, 45° and 90° orientation.

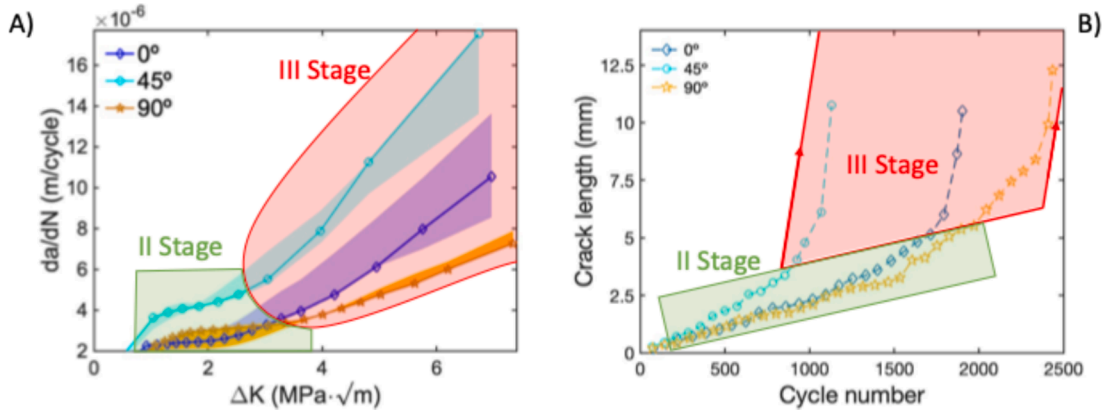

Fig. 9. A) da/dN-Δ*K* curves and B) crack length vs cycle number of 0°, 45° and 90° 18Ni300 samples.

an orientation of 90°, although a greater variability of the aspect ratio is obtained, the pores have smaller areas than in the case of orientations of 0° and 45°. In the case of the 0° orientation, although the aspect ratio remains almost 90 % above 0.85, these pores have a very variable area from 2 to 85 μm^2. Meanwhile, the pores in the 45° orientation have an aspect ratio above 0.85 in 90 % of the pores but are more concentrated below 50 μm^2.

3.3. Fatigue crack growth

In the Paris law regime, cyclic plastic deformation is a widely accepted explanation for FCG. According to Laird's model [37], plastic deformation at the crack tip is highly concentrated along the 45° direction, leading to blunting and the creation of a new fracture surface. The results for the SLM maraging steel exhibit typical linearity and slope in the Paris law regime, indicating that FCG is likely governed by cyclic plastic deformation at the crack tip. SEM analysis of the fracture surface revealed that fatigue crack growth predominantly occurs at the interfaces between layers of the SLM material [21]. When adhesion between the deposited layers is high, failure can occur transgranularly through the grain itself. In many instances, however, failure occurs at the layer boundaries, resulting in steps corresponding to the thickness of one or two grains. Notably, the layer plane being normal to the loading direction is anticipated to have a detrimental effect. The weakness of the interfaces contributes to a relatively tortuous crack path and, consequently, a relatively high fracture surface roughness [38].

To determine the fatigue life of a given material, fatigue crack growth data were collected for the different orientations. Fig. 9 shows the da/dN vs ΔK plots for 0°, 45° and 90° samples. The results depicted in Fig. 9 exhibit solely the second and third fatigue stages, namely growth and fracture, for all the samples tested, due to the specific ΔK values employed during experimentation. The first stage, nucleation, appears to be absent from the results.

Upon closer examination, it is evident that the crack growth rate is higher at an angle of 45° compared to 0° and 90°, Fig. 9. However, a higher da/dN is observed at 0° compared to 90°. This can be attributed to the growth of grain boundaries of the sample, which increases in a cross-section of 45° compared to 90°, and 0° compared to 90° [39]. When the angle is 45°, the microstructure in Fig. 3b reveals a combination of 0° and 90° grains. This combination expands the area of the

Table 3
Paris model fitting.

Orientations	C	m	R^2
0°	$2.275 \cdot 10^{-6} \pm 7.01 \cdot 10^{-9}$	0.171 ± 0.025	0.929 ± 0.047
45°	$3.531 \cdot 10^{-6} \pm 3.08 \cdot 10^{-7}$	0.357 ± 0.046	0.983 ± 0.006
90°	$2.461 \cdot 10^{-6} \pm 2.03 \cdot 10^{-7}$	0.143 ± 0.053	0.989 ± 0.002

MPB where the crack spreads, offering a path with less resistance for crack propagation. The third stage of fatigue occurs in all samples at a certain ΔK value and exhibits a similar slope.

According to the findings presented in Fig. 9, numerous factors contribute to the correlation between the presence of pores depicted in Fig. 5 and the propagation of cracks. First, the correlation between the percentage of surface area occupied by pores and the rate of crack growth is proportional. This means that the higher the surface area of pores, the greater the fatigue crack growth rate is, i.e. for 45° the measured percentage surface area of pores is 0.193 %, while for 0° the surface area covered by pores is 0.159 %. Therefore, a greater surface area indicates that the crack will propagate with a higher rate, as confirmed in Fig. 9. This larger surface area is given by the manufacturing pattern which in the case of 45° is a conjunction between 0° and 90° producing a larger number of pores due to the existence of a larger grain boundary area. Secondly, another factor that affects crack growth is the shape of pores, including circularity and aspect ratio [36]. However, in this work, only the aspect ratio has been found to be related to the fatigue crack growth. Fig. 9 shows a higher growth rate for the 45° sample than for the 0° and 90° sample, which correlates with the aspect ratio distribution shown in Fig. 8, where this parameter is closer to unity. Meaning that the closer aspect ratio is to unity, the higher the fatigue crack growth is. The influence of micro-defects on fatigue performance is widely acknowledged, as outlined in the Z-parameter model [40,41,42], which considers the size, depth, and shape of the defects. Our study reaffirms the crucial role of micro-defect shape in this context. The variations in different orientations are minor, as are the differences in the aspect ratio. Consequently, residual stress may also exert a significant influence on crack propagation performance [43,44].

The second region of the da/dN versus ΔK curves, which represents the stable crack growth phase, has been fitted using the Paris Model, as described by Equation (1). Furthermore, the fitting was performed on data obtained from 3 specimens for each orientation, ensuring that the statistical variability is accounted for. The values presented in Table 3 reflect the mean and standard deviation of the regression parameters. Materials with low values of C and m are generally more resistant to fatigue crack propagation compared to materials with high values. In this case, the II stage is situated between 2 and 6 10^{-6} m/cycle, which represents a relatively high but stable value within the range of 1 to 3 MPa·$\sqrt{m}$. This indicates that the slope is significantly reduced, as depicted in Table 3 for the m parameter. The observed difference can be attributed to the distinct elastic modulus of the printed material in comparison to the bulk material [45]. The Zhu-Xuan model [46,47] could not be further analyzed due to insufficient information in the near-threshold region. Nonetheless, it presents a promising approach for comprehensively describing the influence of load ratio on the fatigue threshold of materials. Additionally, it has been compared with several international standards.

Fig. 10 portrays the trajectory of the crack across the surface of the samples upon the conclusion of stages II and III, during the final cycle of testing. It can be observed that the crack after a certain length starts to follow a curve, Figs. 10a and 10b, or a zigzag, Fig. 10c, which corresponds to entering the III stage of the test. The presence of steeper curves leads to the appearance of surface roughness around the crack.

In the initial stages of crack growth, mode I, result in a linear upward movement by prior observations. However, as demonstrated in Fig. 10a at 0°, the slope continues until the third stage, where the crack deviates from its linear path and begins to follow a curved trajectory, characteristic of the third stage of its progression.

The curved trajectory results from the acceleration of the primary

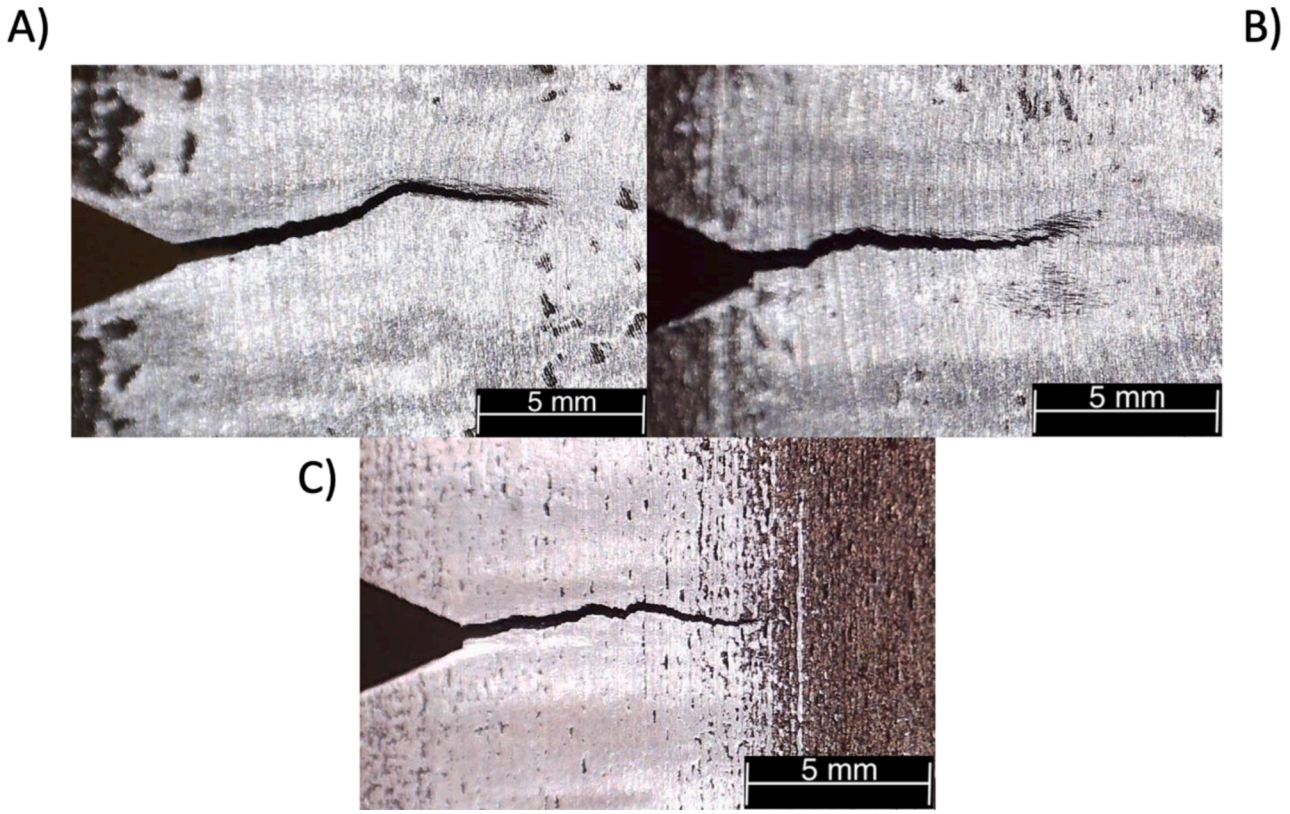

Fig. 10. Fatigue crack profile of samples A) 0°, B) 45° and C) 90°.

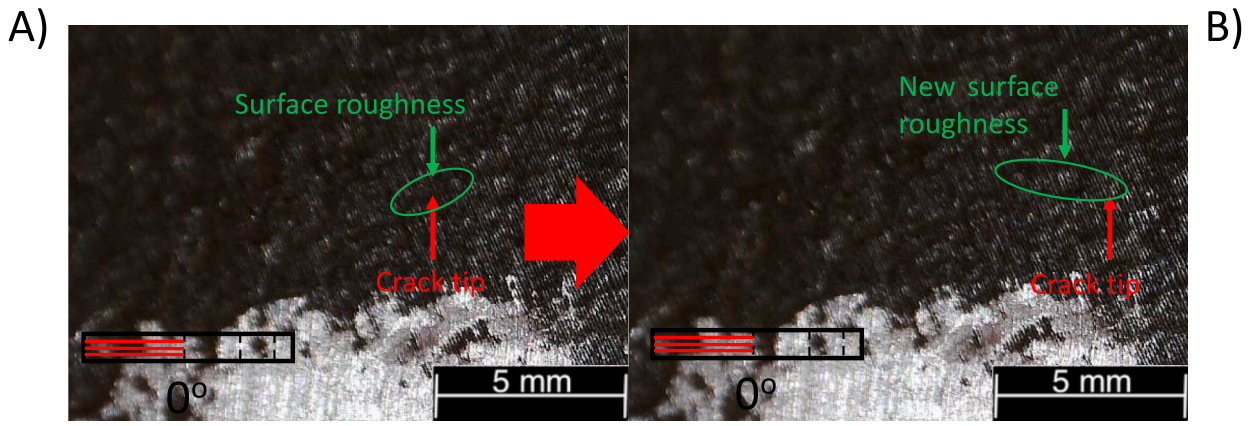

Fig. 11. Third Stage Crack Growth – A) Initiation with Surface Roughness Emerging Ahead of the Crack Tip, and B) Growth with Increasing Surface Roughness Thickness as the Crack Tip Advances.

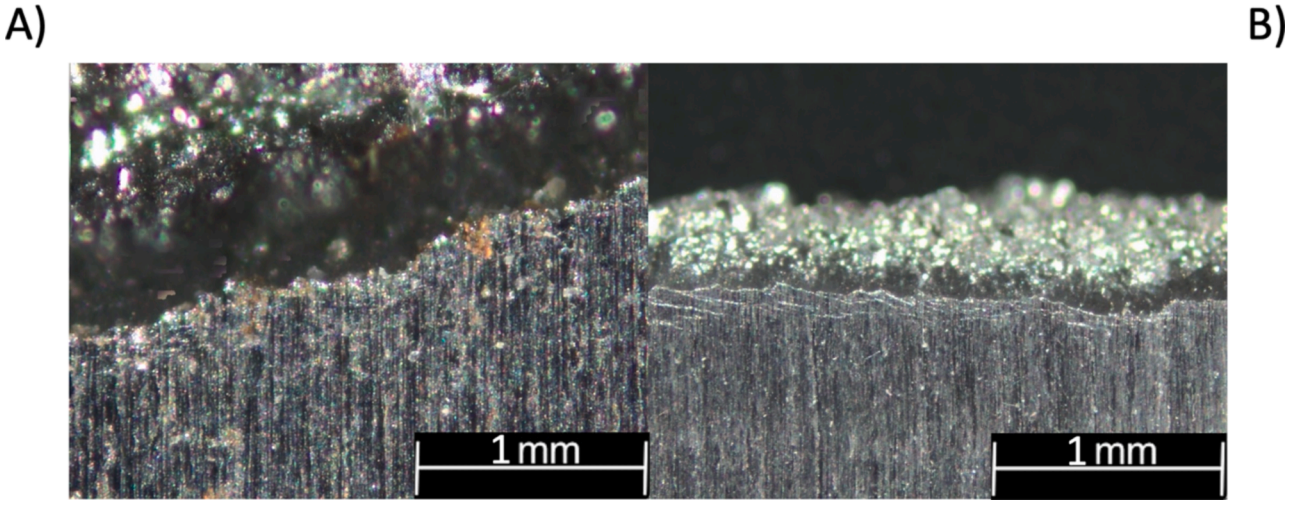

Fig. 12. Surface Edge side view of Additive Manufactured CT Specimen Crack, A) 0° and B) 45°.

crack due to the surface roughness appearing ahead of the primary crack, Fig. 11. The appearance of the surface roughness is limited to the 0° and 45° samples due to the fabrication process, which creates a higher porosity area inside the samples and potentially leads to a redistribution of stress, causing deviation from mode I loading.

A minor fracture emerged at a 45° angle in Fig. 10b, adjacent to the primary fracture, following a brief period of growth. As the stress intensity factor range increased, the small crack produced by the surface roughness merged with the primary crack, leading to a surge in the crack propagation rate [48]. This phenomenon was observed at a later stage in Fig. 10a and 10b. Additionally, Fig. 10c demonstrated a more extended period of fracture growth at a 90° angle, culminating in the reappearance of the earlier curvature.

The surface roughness is not present on the faces in the initial stages of Fig. 10a and 10b. It becomes noticeable only when the small crack merges with the main one. Conversely, in Fig. 10c, the main crack extends without any surface roughness due to the absence of secondary cracks.

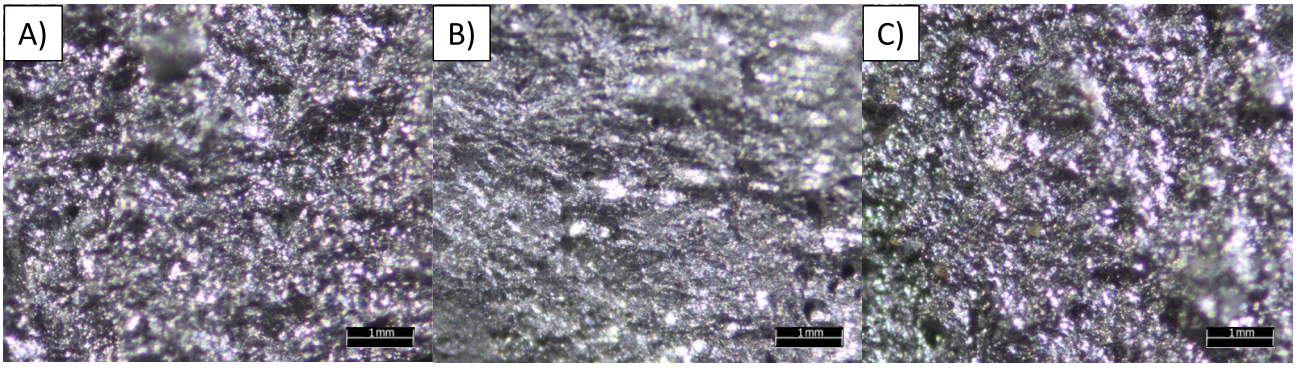

Fig. 13. Fractography of the CT specimens A) 0°, B) 45° and C) 90°.

3.4. Fracture surface analysis

The initiation of the third stage of crack growth is shown in Fig. 11, where the surface roughness appears and the third fatigue stage starts. In Fig. 11a, the surface is illustrated just before the onset of the third phase, with the surface roughness becoming perceptible ahead of the crack tip. This observation suggests that the presence of surface roughness accelerates the rate of crack growth. Conversely, Fig. 11b, which represents an advanced stage of the third stage, shows that the surface roughness is only in this stage and when it is more advanced, the surface roughness layer is thicker. The difference between the edges of the 0° and 45° samples can be seen without the need for a microscope, Fig. 10a and 10b. Fig. 12a shows more blunted edges of the crack, meaning a smoother crack growth that corresponds to the crack growing second stage. Meanwhile, in Fig. 12b, sharper ridges represent faster cracking due to shorter periods of the appliance of forces. This is a characteristic in the third stage of fatigue cracking, where the propagation rate of the crack is higher. Fig. 13 shows the fractography of the three orientations. No clear variation was observed between the 0° (Fig. 13.A), 45° (Fig. 13.B) and 90° (Fig. 13.C) manufacturing orientations in terms of morphology and surface roughness.

4. Conclusions

As part of our ongoing research efforts, a study was conducted to evaluate the fatigue performance and crack propagation behaviour of samples composed of SLM maraging steel. Specifically, samples with printing directions of 0°, 45°, and 90° were examined. The analysis examined how the fatigue properties of SLM samples were affected by the printing directions used. Through rigorous testing and thoughtful discussion, we were able to draw valuable insights and conclusions as follows.

The way the samples were made affects significantly how cracks spread. Areas with high strain concentration, like the MPBs or porosity, are more susceptible to crack propagation. Based on the results of the current work, several crucial conclusions can be drawn, namely:

1. The crack growth rate is affected by the size of the pore area, as larger pore areas accelerate crack growth due to higher aspect ratios. While the pores in different orientations share similar unit area and diameter, the aspect ratio plays a role in influencing crack growth. This observation was made during the 45° orientation test.
2. The circularity ratio exerts varying influences on stress concentrators, with higher stress concentration observed in 0° and 45° orientations for more spherical pores.
3. The highest crack growth rate occurs at an angle of 45°, corresponding to the maximum area of porous and MPBs where the crack can grow. This geometry also reveals the greater porosity area, and this porosity has a higher aspect ratio, which affects directly the rate.
4. The research shows that the third stage of fatigue is achieved when the secondary crack merges with the primary crack, leading to the deformation of the surface of the samples.

CRediT authorship contribution statement

Pablo M. Cerezo: Writing – original draft, Visualization, Validation, Methodology, Formal analysis. **Alejandro S. Cruces:** Writing – review & editing, Supervision, Software, Resources, Project administration, Investigation, Data curation, Conceptualization. **Steven Moore:** Writing – review & editing, Methodology, Data curation. **Greg Wheatley:** Writing – review & editing, Validation, Supervision, Investigation, Funding acquisition, Formal analysis, Data curation. **Pablo Lopez-Crespo:** Writing – review & editing, Writing – original draft, Validation, Supervision, Resources, Project administration, Methodology, Investigation, Funding acquisition, Data curation, Conceptualization.

Declaration of competing interest

The authors declare that they have no known competing financial interests or personal relationships that could have appeared to influence the work reported in this paper.

Acknowledgement

The authors would like to acknowledge the financial support of Programa Operativo FEDER from Junta de Andalucia (Spain) through grant reference UMA18-FEDERJA-250. The authors would also like to acknowledge funding for open access charge: Universidad de Malaga / CBUA.

Data availability

Data will be made available on request.

References

[1] N. Sanaei, A. Fatemi, Defects in additive manufactured metals and their effect on fatigue performance: A state-of-the-art review, Prog. Mater. Sci 117 (Apr. 2021) 100724, https://doi.org/10.1016/j.pmatsci.2020.100724.
[2] T. Wohlers, et al., History of Additive Manufacturing, SSRN Electron. J. (2023), https://doi.org/10.2139/ssrn.4474824.
[3] S. Liu, Y.C. Shin, Additive manufacturing of Ti6Al4V alloy: A review, Mater Des 164 (Feb. 2019) 107552, https://doi.org/10.1016/j.matdes.2018.107552.
[4] P. Li, D.H. Warner, A. Fatemi, N. Phan, Critical assessment of the fatigue performance of additively manufactured Ti–6Al–4V and perspective for future research, Int. J. Fatigue 85 (Apr. 2016) 130–143, https://doi.org/10.1016/j.ijfatigue.2015.12.003.
[5] A.S. Cruces, R. Branco, L.P. Borrego, P. Lopez-Crespo, Energy-based critical plane fatigue methods applied to additively manufactured 18Ni300 steel, Int. J. Fatigue 170 (May 2023) 107548, https://doi.org/10.1016/j.ijfatigue.2023.107548.
[6] R. Caivano, A. Tridello, G. Chiandussi, G. Qian, D. Paolino, F. Berto, Very high cycle fatigue (VHCF) response of additively manufactured materials: A review, Fatigue Fract. Eng. Mater. Struct. 44 (11) (Nov. 2021) 2919–2943, https://doi.org/10.1111/ffe.13567.
[7] Z.H. Jiao, L.M. Lei, H.C. Yu, F. Xu, R.D. Xu, X.R. Wu, Experimental evaluation on elevated temperature fatigue and tensile properties of one selective laser melted nickel based superalloy, Int J Fatigue 121 (Apr. 2019) 172–180, https://doi.org/10.1016/j.ijfatigue.2018.12.024.
[8] L.M.S. Santos, L.P. Borrego, J.A.M. Ferreira, J. de Jesus, J.D. Costa, C. Capela, Effect of heat treatment on the fatigue crack growth behaviour in additive manufactured AISI 18Ni300 steel, Theor. Appl. Fract. Mech. 102 (Aug. 2019) 10–15, https://doi.org/10.1016/j.tafmec.2019.04.005.
[9] R. Branco et al., 'Low-Cycle Fatigue Behaviour of AISI 18Ni300Maraging Steel Produced by Selective Laser Melting', Technology (Singap World Sci), p. 7491, doi: 10.3390/met8010032.
[10] J. Fikes, 'Rapid Analysis & Manufacturing Propulsion Technology', 2019.
[11] A.S. Cruces, A. Exposito, R. Branco, L.P. Borrego, F.V. Antunes, P. Lopez-Crespo, Study of the notch fatigue behaviour under biaxial conditions of maraging steel produced by selective laser melting, Theor. Appl. Fract. Mech. 121 (Oct. 2022) 103469, https://doi.org/10.1016/j.tafmec.2022.103469.
[12] A.F. Chadwick, P.W. Voorhees, The development of grain structure during additive manufacturing, Acta Mater 211 (Jun. 2021) 116862, https://doi.org/10.1016/j.actamat.2021.116862.
[13] Y. Bai, C. Zhao, J. Yang, R. Hong, C. Weng, H. Wang, Microstructure and machinability of selective laser melted high-strength maraging steel with heat treatment, J Mater Process Technol 288 (Feb. 2021) 116906, https://doi.org/10.1016/j.jmatprotec.2020.116906.
[14] J. Mutua, S. Nakata, T. Onda, Z.-C. Chen, Optimization of selective laser melting parameters and influence of post heat treatment on microstructure and mechanical properties of maraging steel, Mater Des 139 (Feb. 2018) 486–497, https://doi.org/10.1016/j.matdes.2017.11.042.
[15] C. Tan, K. Zhou, M. Kuang, W. Ma, T. Kuang, Microstructural characterization and properties of selective laser melted maraging steel with different build directions, Sci Technol Adv Mater 19 (1) (Dec. 2018) 746–758, https://doi.org/10.1080/14686996.2018.1527645.
[16] L. Wu, Z. Jiao, H. Yu, Study on fatigue crack growth behavior of selective laser-melted Ti6Al4V under different build directions, stress ratios, and temperatures, Fatigue Fract Eng Mater Struct 45 (5) (May 2022) 1421–1434, https://doi.org/10.1111/ffe.13670.
[17] J. N. Domfang Ngnekou et al., 'Fatigue properties of AlSi10Mg produced by Additive Layer Manufacturing', Int J Fatigue, vol. 119, pp. 160–172, Feb. 2019, doi: 10.1016/J.IJFATIGUE.2018.09.029.
[18] K. Solberg, E.W. Hovig, K. Sørby, F. Berto, Directional fatigue behaviour of maraging steel grade 300 produced by laser powder bed fusion, Int J Fatigue 149 (Aug. 2021), https://doi.org/10.1016/J.IJFATIGUE.2021.106229.

[19] N. Chawla, X. Deng, Microstructure and mechanical behavior of porous sintered steels, Mater. Sci. Eng. A 390 (1–2) (Jan. 2005) 98–112, https://doi.org/10.1016/J.MSEA.2004.08.046.
[20] F. Léonard, S. Tammas-Williams, and I. Todd, 'CT for Additive Manufacturing Process Characterisation: Assessment of melt strategies on defect population', in In 6th conference on industrial computed tomography, 2016, pp. 9–12.
[21] J. Suryawanshi, K.G. Prashanth, U. Ramamurty, Tensile, fracture, and fatigue crack growth properties of a 3D printed maraging steel through selective laser melting, J Alloys Compd 725 (Nov. 2017) 355–364, https://doi.org/10.1016/j.jallcom.2017.07.177.
[22] L.M.S. Santos, J.A.M. Ferreira, L.P. Borrego, J.D. Costa, C. Capela, J. de Jesus, Fatigue crack propagation along interfaces of selective laser melting steel hybrid parts, Fatigue Fract Eng Mater Struct 42 (11) (Nov. 2019) 2431–2440, https://doi.org/10.1111/ffe.13072.
[23] Z. Zhao, et al., Influence of pore defects on the mechanical property and corrosion behavior of SLM 18Ni300 maraging steel, Mater. Charact. 182 (Dec. 2021) 111514, https://doi.org/10.1016/j.matchar.2021.111514.
[24] A. S. Cruces, P. Lopez-Crespo, R. Branco, B. Moreno, and L. Borrego, 'PROPAGACIÓN DE GRIETAS DE FATIGA DESDE CONCENTRADOR EN ACERO MARAGING BAJO CARGAS DE TIPO BIAXIAL'.
[25] ASM International Handbook Committee, 'Properties and Selection: irons Steels and High-Performance Alloys', ASM Handbook, 1991.
[26] C. Tan et al., 'Microstructure and Mechanical Properties of 18Ni-300 Maraging Steel Fabricated by Selective Laser Melting', in Proceedings of the 2016 6th International Conference on Advanced Design and Manufacturing Engineering (ICADME 2016), Paris, France: Atlantis Press, 2016, pp. 404–410. doi: 10.2991/icadme-16.2016.66.
[27] G. Casalino, S.L. Campanelli, N. Contuzzi, A.D. Ludovico, Experimental investigation and statistical optimisation of the selective laser melting process of a maraging steel, Opt. Laser Technol. 65 (Jan. 2015) 151–158, https://doi.org/10.1016/j.optlastec.2014.07.021.
[28] D. Croccolo, M. De Agostinis, S. Fini, G. Olmi, A. Vranic, S. Ciric-Kostic, Influence of the build orientation on the fatigue strength of EOS maraging steel produced by additive metal machine, Fatigue Fract. Eng. Mater. Struct. 39 (5) (May 2016) 637–647, https://doi.org/10.1111/ffe.12395.
[29] F. Tariq, N. Naz, R.A. Baloch, Effect of cyclic aging on mechanical properties and microstructure of maraging steel 250, J. Mater. Eng. Perform. 19 (7) (Oct. 2010) 1005–1014, https://doi.org/10.1007/s11665-009-9583-7.
[30] 'Introduction to additive manufacturing technology, a guide for designers and engineers', European Powder Metallurgy Association., 2015.
[31] W. Wu, et al., Microstructure and mechanical properties of maraging 18Ni-300 steel obtained by powder bed based selective laser melting process, Rapid Prototyp J 26 (8) (Jun. 2020) 1379–1387, https://doi.org/10.1108/RPJ-08-2018-0189.
[32] ASTM International Committee E08 on Fatigue and Fracture. Subcommittee E08.07 on Fracture Mechanics, 'Standard Test Method for Linear-elastic Plane-strain Fracture Toughness K [Ic] of Metallic Materials', ASTM international, 2013.
[33] A.S.T.M. Committee, E-4 on Metallography, 'Standard Practice for Microetching Metals and Alloys', ASTM International (2013).
[34] J.R. Davis, Metals Handbook: Structure/property Relationships in Irons and Steels. (1998).
[35] H.C. Pavanati, A.M. Maliska, A.N. Klein, J.L.R. Muzart, Comparative study of porosity and pores morphology of unalloyed iron sintered in furnace and plasma reactor, Mater. Res. 10 (1) (2007) 87–93, https://doi.org/10.1590/S1516-14392007000100019.
[36] S. Tammas-Williams, P.J. Withers, I. Todd, P.B. Prangnell, The Influence of Porosity on Fatigue Crack Initiation in Additively Manufactured Titanium Components, Sci Rep 7 (1) (Aug. 2017) 7308, https://doi.org/10.1038/s41598-017-06504-5.
[37] C. Laird, G.C. Smith, Initial stages of damage in high stress fatigue in some pure metals, Phil. Mag. 8 (95) (Nov. 1963) 1945–1963, https://doi.org/10.1080/14786436308209084.
[38] F. Antunes, et al., Fatigue Crack Growth in Maraging Steel Obtained by Selective Laser Melting, Appl. Sci. 9 (20) (Oct. 2019) 4412, https://doi.org/10.3390/app9204412.
[39] Z. Xu, A. Liu, X. Wang, Fatigue performance and crack propagation behavior of selective laser melted AlSi10Mg in 0°, 15°, 45° and 90° building directions, Mater. Sci. Eng. A 812 (Apr. 2021) 141141, https://doi.org/10.1016/j.msea.2021.141141.
[40] G. Zhu, Y.-C. Wu, M.-L. Zhu, F.-Z. Xuan, Towards a general damage law for interior micro-defect induced fatigue cracking in martensitic steels, Int J Fatigue 153 (Dec. 2021) 106501, https://doi.org/10.1016/j.ijfatigue.2021.106501.
[41] M. Zhu, G. Zhu, F. Xuan, On micro-defect induced cracking in very high cycle fatigue regime, Fatigue Fract Eng Mater Struct 45 (11) (Nov. 2022) 3393–3402, https://doi.org/10.1111/ffe.13793.
[42] M.-L. Zhu, L. Jin, F.-Z. Xuan, Fatigue life and mechanistic modeling of interior micro-defect induced cracking in high cycle and very high cycle regimes, Acta Mater 157 (Sep. 2018) 259–275, https://doi.org/10.1016/j.actamat.2018.07.036.
[43] P.J. Withers, H.K.D.H. Bhadeshia, Residual stress. Part 2 – Nature and origins, Materials Science and Technology 17 (4) (Apr. 2001) 366–375, https://doi.org/10.1179/026708301101510087.
[44] W. Chen, et al., Microscale residual stresses in additively manufactured stainless steel, Nat Commun 10 (1) (Sep. 2019) 4338, https://doi.org/10.1038/s41467-019-12265-8.
[45] M. Ciavarella, M. Paggi, A. Carpinteri, One, no one, and one hundred thousand crack propagation laws: A generalized Barenblatt and Botvina dimensional analysis approach to fatigue crack growth, J Mech Phys Solids 56 (12) (Dec. 2008) 3416–3432, https://doi.org/10.1016/j.jmps.2008.09.002.
[46] B.-B. Zhuang, Y.-X. Liu, Y.-N. Du, M.-L. to exa, and F.-Z. Xuan, 'A new bilinear model for fatigue crack growth evaluation', International Journal of Pressure Vessels and Piping, vol. 200, p. 104850, Dec. 2022, doi: 10.1016/j.ijpvp.2022.104850.
[47] M.-L. Zhu, F.-Z. Xuan, S.-T. Tu, Effect of load ratio on fatigue crack growth in the near-threshold regime: A literature review, and a combined crack closure and driving force approach, Eng Fract Mech 141 (Jun. 2015) 57–77, https://doi.org/10.1016/j.engfracmech.2015.05.005.
[48] D.D. Ben, et al., Heterogeneous microstructure and voids dependence of tensile deformation in a selective laser melted AlSi10Mg alloy, Mater. Sci. Eng. A 798 (Nov. 2020) 140109, https://doi.org/10.1016/j.msea.2020.140109.